Dalton Transactions

ROYAL SOCIETY OF CHEMISTRY

PAPER

View Article Online
View Journal | View Issue

Cite this: *Dalton Trans.*, 2024, **53**, 12291

Construction of hierarchical In_2O_3/In_2S_3-ZnCdS ternary microsphere heterostructures for efficient photocatalytic nitrogen fixation†

Liangliang Huang, Tao Peng, Rui Wang, Beibei He, Jun Jin, Huanwen Wang and Yansheng Gong *

Photocatalytic ammonia production holds immense promise as an environmentally sustainable approach to nitrogen fixation. In this study, In_2O_3/In_2S_3-ZnCdS ternary heterostructures were successfully constructed through an innovative in situ anion exchange process, coupled with a low-temperature hydrothermal method for ZnCdS (ZCS) incorporation. The resulting In_2O_3/In_2S_3-ZCS photocatalyst was proved to be highly efficient in converting N_2 to NH_3 under mild conditions, eliminating the need for sacrificial agents or precious metal catalysts. Notably, the NH_4^+ yield of In_2O_3/In_2S_3-0.5ZCS reached a significant level of 71.2 μmol g^{-1} h^{-1}, which was 10.47 times higher than that of In_2O_3 (6.8 μmol g^{-1} h^{-1}) and 3.22 times higher than that of In_2O_3/In_2S_3 (22.1 μmol g^{-1} h^{-1}). This outstanding performance can be attributed to the ternary heterojunction configuration, which significantly extends the lifetime of photogenerated carriers and enhances the spatial separation of electrons and holes. The synergistic interplay between CdZnS, In_2S_3, and In_2O_3 in the heterojunction facilitates electron transport, thereby boosting the rate of the photocatalytic nitrogen fixation reaction. Our study not only validates the efficacy of ternary heterojunctions in photocatalytic nitrogen fixation but also offers valuable insights for the design and construction of such catalysts for future applications.

Received 2nd June 2024,
Accepted 1st July 2024

DOI: 10.1039/d4dt01605j

rsc.li/dalton

1. Introduction

Nitrogen, renowned as an indispensable component of nature, comprises a significant 78% of the atmosphere's total volume, making it the most abundant gas.[1–3] On the other hand, ammonia stands as a clean and efficient energy source, crucial in modern industry, agriculture and energy storage.[4] Its low liquefaction pressure and high hydrogen density contribute significantly to its vital role.[5] Consequently, the conversion of N_2 to NH_3 has attracted much attention. In 1916, the Haber–Bosch process emerged as the sole industrial method for this conversion.[6,7] However, this process requires stringent conditions, including temperatures ranging from 400–600 °C and pressures of 20–40 MPa,[8,9] leading to substantial fossil energy consumption and greenhouse gas emissions.[10,11] Therefore it is imperative to explore a novel ammonia synthesis process that is energy-efficient, environmentally friendly, and mild in operating conditions.

In recent decades, the photocatalytic ammonia synthesis process has emerged as a promising alternative.[12,13] This method enables the direct reaction of water as a source of H_2 with N_2 to produce ammonia under ambient temperature and pressure conditions. Notably, it stands as an environmentally friendly technology, characterized by low energy consumption, safe operation, and zero pollution.[14–16] At present, many photocatalysts, such as bismuth-based photocatalysts (Bi_2MoO_6),[17] titanium-based photocatalysts (TiO_2),[18] and carbon-based photocatalysts (g-C_3N_4),[19] have garnered widespread attention due to their remarkable stability, cost-effectiveness, low toxicity, high efficiency, and broad visible-light response range. Consequently, these photocatalysts have been extensively utilized in photocatalytic nitrogen fixation reactions.[20]

As an n-type semiconductor photocatalyst,[21] indium oxide (In_2O_3) possesses excellent electrical conductivity and thermodynamic stability,[22,23] garnering significant attention in the realm of photoelectrochemistry.[24] Though its positive valence band potential renders it active in the degradation of organic molecules,[25] its relatively low conduction band potential limits its effectiveness in nitrogen fixation.[26] Furthermore, the photocatalytic performance of In_2O_3 is hampered by the high rate of recombination of photoexcited

Faculty of Materials Science and Chemistry, China University of Geosciences, Wuhan 430074, P. R. China. E-mail: gongysh@cug.edu.cn; Fax: +86 027 6788 3731; Tel: +86 027 6788 3731

† Electronic supplementary information (ESI) available. See DOI: https://doi.org/10.1039/d4dt01605j

electrons and holes, as well as the low utilization rate of solar photons,[27,28] necessitating modifications to enhance its efficiency. Common strategies for modifying In_2O_3 include doping with metal/non-metal atoms, altering its morphology, and constructing heterojunction and defects.[29] Notably, the design of a heterojunction structure by combining two semiconductors with interleaved energy band structures facilitates the effective separation of photogenerated electron–hole pairs, enabling superior redox reactions on the catalyst's active sites. Metal sulfide semiconductors have garnered significant interest in photocatalytic nitrogen fixation owing to their exceptional light absorption capabilities and relatively negative reduction potential positions.[30,31] Among various metal sulfides, indium sulphide (In_2S_3) stands out as an n-type semiconductor that boasts high photosensitivity, photoconductivity, chemical stability and efficient utilization of light energy.[32,33] Until now, numerous In_2O_3/In_2S_3 composites have been successfully implemented in photocatalytic applications. For instance, Xu *et al.* presented a report on In_2O_3/In_2S_3 microspherical heterostructures crafted through a two-step hydrothermal process, exhibiting remarkable efficacy in nitrogen fixation.[34] Furthermore, the CdZnS solid solution stands out for its unique structure, a lower rate of photogenerated carrier complexation, and adjustable energy bands,[35,36] distinguishing it from conventional CdS. This grants it superior photocatalytic performance in response to light, making it suitable for a wide array of applications in the photocatalytic realm of applications in the photocatalytic field. For example, Zhang *et al.* discovered that N–C/CdZnS/In_2O_3 heterojunction photocatalysts exhibited excellent hydrogen precipitation performance.[37]

In the photocatalytic nitrogen fixation process, sacrificial agents are often added to promote charge separation and enhance the photocatalytic activity. The primary techniques for the detection of ammonia yield include salicylic acid spectrophotometry, Nessler's reagent spectrophotometry and ion chromatography.[38] Especially, Nessler's reagent spectrophotometry is widely used due to its high sensitivity, convenient operation and precision. However, the addition of the sacrificial agent may introduce inaccuracies Nessler's reagent detection.[39]

Based on the above analysis, In_2O_3 microspheres were firstly synthesized through a straightforward hydrothermal calcination process. Subsequently, In_2O_3/In_2S_3 composites were prepared via a rapid and efficient in situ anion-exchange method, utilizing In_2O_3 as the base material and L-cysteine as the sulfur source. The synergistic interaction between In_2O_3 and In_2S_3 effectively facilitates the transfer and spatial separation of photogenerated carriers, thereby promoting the photocatalytic nitrogen fixation performance. In addition, ZnCdS nanoparticles were uniformly deposited on the surface of In_2O_3/In_2S_3 via a simple hydrothermal process, creating an In_2O_3/In_2S_3-ZCS heterostructure. Overall, a two-step refinement of In_2O_3 was carried out, and in the absence of sacrificial agent, the NH_4^+ yield attained 71.2 μmol g^{-1} h^{-1} upon the addition of 50 wt% ZCS, which is 10.47 times higher than that of In_2O_3 (6.8 μmol g^{-1} h^{-1}) and 3.22 times higher than that of In_2O_3/In_2S_3 (22.1 μmol g^{-1} h^{-1}).

2. Experimental section

2.1 Chemicals and materials

Indium chloride ($InCl_3$, 99.9% metals basis), sodium dodecyl sulfate (SDS, $C_{12}H_{25}NaO_4S$, AR), urea ($CO(NH_2)_2$, 99%), L-cysteine ($C_3H_7NO_2S$, 99%), thiourea (CH_4N_2S, AR) were purchased from Aladdin Industrial Corporation. Zinc acetate dihydrate ($(CH_3COO)_2Zn{\cdot}2H_2O$, AR), and cadmium acetate dihydrate ($(CH_3COO)_2Cd{\cdot}2H_2O$, AR) were purchased from Sinopharm Chemical Reagent. All the experimental reagents used directly without any further purification. N_2 (99.999%) and Ar (99.999%) were purchased from Wuhan Iron and Steel Group. Deionized water (18.2 MΩ) was used in all the experiments.

2.2 Preparation of In_2O_3

Initially, 0.884 g (4 mmol) of $InCl_3$ and 3.46 g (12 mmol) of sodium dodecyl sulfate were dispersed in 60 ml of high-purity water. Subsequently, 2.4 g (40 mmol) of urea was added to the mixed solution, and stirring was maintained for 3 h. Following this, the resulting suspension was transferred to a 100 mL Teflon-lined autoclave and reacted at 120 °C for 12 h. After cooling to room temperature, the precipitate was collected by centrifugation and thoroughly washed with ultrapure water several times. The collected solid was then dried in a vacuum freeze dryer for 24 h to obtain the precursor $In(OH)_3$. Subsequently, $In(OH)_3$ was calcined at 400 °C for 2 h at a heating rate of 5 °C per minute, and cooled to room temperature to obtain light yellow spherical flower-like In_2O_3.

2.3 Preparation of In_2O_3/In_2S_3

To prepare the desired mixture, 8 mg of L-cysteine was introduced into 20 ml of high-purity water. The solution was thoroughly stirred for an hour to ensure the complete dissolution. Subsequently, 0.4 g of In_2O_3 were added and vigorously mixed for another 4 h. Once the reaction was complete, the resulting product underwent centrifugation and was thoroughly washed with deionized water and anhydrous ethanol, repeated multiple times.

2.4 Preparation of In_2O_3/In_2S_3-$Zn_{0.4}Cd_{0.6}S$

Typically, to synthesize In_2O_3/In_2S_3-0.5ZCS, containing 50 wt% of $Zn_{0.4}Cd_{0.6}S$, 0.2 g of In_2O_3/In_2S_3 was first dissolved in 60 ml of high purity water. Subsequently, 0.1 g of zinc acetate dihydrate and 0.18 g of cadmium acetate dihydrate was added to the solution and sonicated for 10 min to achieve a homogeneous dispersion. After this, 0.1 g of thiourea was incorporated and the mixture was stirred at room temperature for 1 h. Following this, the suspension was reacted in a 100 mL Teflon-lined autoclave at 80 °C for 2 h. To purify the product, it was centrifuged and washed multiple times with deionized water and ethanol. Finally, the resulting material was dried in a vacuum oven at 60 °C for 12 h to obtain In_2O_3/In_2S_3-0.5ZCS.

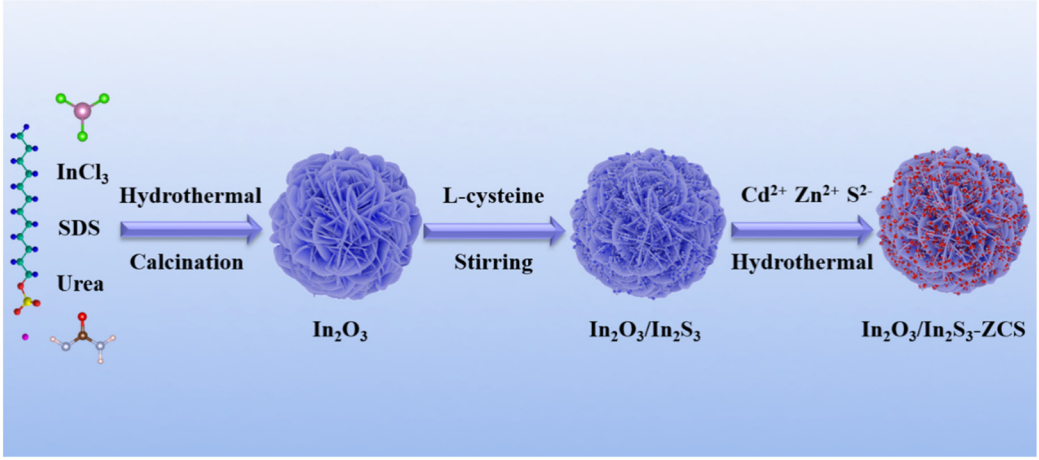

Scheme 1 Schematic route for the synthesis of heterostructure of In_2O_3/In_2S_3-ZCS microspheres.

The preparation of In_2O_3/In_2S_3-0.4ZCS and In_2O_3/In_2S_3-0.6ZCS, containing 40% and 60% by weight of $Zn_{0.4}Cd_{0.6}S$, respectively, followed similar procedures. The entire process is illustrated in Scheme 1.

2.5 Characterization

The crystalline structure of the as-prepared samples was recorded by X-ray diffraction (XRD, D8-FOCUS, Bruker AXS, Panalytical). X-ray photoelectron spectroscopy (XPS, Escalab 250XI, ThermoFisher) was used to analyze the surface elemental composition and chemical states of samples with Al Kα monochromatized radiations. Scanning electronic microscopy (SEM, SU3500, Japan) and transmission electron microscope (TEM, Journal FEI Talos F200S) was used to observe the morphology and composition structure. N_2 adsorption/desorption analysis was conducted by Micromeritics ASAP2460 surface area analyzer at 77 K. UV-vis DRS of the samples was measured on a UV-vis diffuse reflectance spectrometer (Lambda35, PerkinElmer). The PL spectra of the samples were obtained using an Edinburgh FLS980 spectrophotometer (PANalytical, Axios) at an excitation wavelength of 370 nm at room temperature.

2.6 Photoelectrochemical measurements

Electrochemical impedance spectroscopy (EIS), photocurrent test was performed on a CHI760E Electrochemical Workstation (Chenhua Instrument Co. Shanghai). A standard three-electrode system was used in all the tests using 0.5 M Na_2SO_4 solution as an electrolyte. Platinum wire was used as the counter electrode, while Ag/AgCl (saturated KCl) electrode was employed as the reference electrode. The working electrode was composed of the as-prepared samples loaded on FTO glass. The working electrode was prepared as follows: 5 mg photocatalyst was added to 300 μL anhydrous ethanol and dispersed for 3 h. After that, 10 μL Nafion solution (5 wt%) was added to obtain a well-dispersed slurry with a certain viscosity. The above-mentioned 60 μL slurry was uniformly coated onto FTO glass (10 mm × 40 mm) with 10 mm × 10 mm sections. Afterward, the coated conductive glass was dried overnight at room temperature to produce a working electrode. The photocurrent test was carried out at 0 V *vs.* Ag/AgCl with an on/off cycle of 30 s. EIS tests were performed under open circuit potential conditions using frequencies from 10^{-2} to 10^5 Hz.

2.7 Photocatalytic activity measurement

The photocatalytic N_2 reduction reaction (NRR) test is carried out in a double-layer quartz reactor. In a typical experiment, 100 mL water and 50 mg photocatalyst were added to a 200 mL quartz reactor and sonicated for 5 min to obtain a well-dispersed suspension. Before the photocatalytic reaction, dissolved oxygen was removed from the suspension by stirring for 30 min under the dark condition with a constant flow of nitrogen (200 mL min^{-1}). A 300 W Xe lamp was used for illumination, and the distance from the light source to the liquid level was kept at 10 cm. The nitrogen was bubbled into the suspension at a flow rate of 200 ml min^{-1} throughout the photocatalytic nitrogen fixation process, and the temperature of the reaction system was maintained at 20 °C using a circulating cooling system. The yield of NH_4^+ was evaluated by using Nessler's reagent spectrophotometry (HJ 535-2009). In simple terms, the catalyst was filtered through a disposable needle filter (0.22 μm) at regular intervals, and a clarified 5 mL solution was taken into a colorimetric tube. Subsequently, 100 μL potassium sodium tartrate solution to the colorimetric tube, followed by 100 μL Nessler's reagent. The mixture was allowed to stand for 30 min and then analyzed for the absorbance at 420 nm using a fiber optic spectrometer, employing deionized water as the reference. Parallelly, the cycling stability of 50 mg of the photocatalyst was evaluated under identical conditions. After each photocatalytic reaction, the reaction liquid was filtered out, and the photocatalyst was thoroughly washed three times with deionized water and dried in an oven at 60 °C for 12 h before the next test. The apparent quantum yields (AQY) were tested under a 300 W Xe lamp, utilizing various UV-vis

filters (420 nm, 450 nm and 500 nm), and the results were calculated employing eqn (1). The average irradiation intensities were measured to be 4.5 mW cm^{-2} at 420 nm, 3.8 mW cm^{-2} at 450 nm and 5.1 mW cm^{-2} at 500 nm, respectively.

$$\mathrm{AQY} = \frac{3 \times \text{number of ammonia molecules}}{\text{number of incident photons}} \times 100\% \quad (1)$$

3. Results and discussion

3.1 Structure and composition

The crystal structure and phase composition of the prepared samples were characterized using X-ray diffraction (XRD), as shown in Fig. 1a. Prominent diffraction peaks at 2θ angles of 30.8°, 35.5°, 51.5° and 60.8° in all the samples are attributed to the (222), (400), (440), and (622) crystal planes of In_2O_3, aligning with the standard card (JCPDS No.06-0416). In the In_2O_3/In_2S_3 map, there are no apparent characteristic peaks of In_2S_3, likely due to the low addition of L-cysteine (2% addition) and high dispersion.[40] Fig. 1b shows a magnified view of 2θ between 29.0° and 32.5°, revealing that the peaks of the In_2O_3/In_2S_3-ZCS pattern exhibit a leftward shift, because the ZnCdS has a characteristic peak at 27.4° corresponding to the (111) crystal plane. Therefore, the successful loading of the ZnCdS particles onto the In_2O_3/In_2S_3 likely results in the overlap of diffraction peaks towards the left. Fig. S1† shows the physical drawings of all the samples, where pure In_2O_3 appears as a yellowish powder, In_2O_3/In_2S_3 as yellow-green, and In_2O_3/In_2S_3-ZCS transitions to an orange-yellow hue upon ZnCdS loading. As the ZnCdS loading ratio increases, the color becomes more yellow and uniform, indicating to a certain degree, the successful combination of In_2S_3 and ZnCdS.

The surface elemental composition and electronic structure of the samples In_2O_3, In_2O_3/In_2S_3, and In_2O_3/In_2S_3-0.5ZCS were further investigated using XPS. Fig. 2a demonstrates the full spectrum of In_2O_3/In_2S_3-0.5ZCS, clearly indicating the presence of the elements of In, O, S, Cd, and Zn. Fig. 2(b–f) further illustrate the high-resolution spectra of In 3d, O 1s, S 2p, Cd 3d, and Zn 2p, respectively. As depicted in Fig. 2b, In 3d spectrum in In_2O_3 can be divided into two main peaks with binding energies of about 444.56 eV and 452.06 eV, corresponding to In $3d_{5/2}$ and In $3d_{3/2}$, respectively. However, after anion-exchange *in situ* growth of In_2S_3, these binding energies underwent a notable shift to lower values of 444.40 eV and 451.96 eV. In (Fig. 2c), two asymmetric peaks of O 1s in In_2O_3 are observed. One peak, with a binding energy of 531.09 eV, signifies the presence of O atoms associated with oxygen vacancies. The other peak, at 529.80 eV, originates from lattice oxygen. Notably, after the in situ growth of In_2S_3, the peak associated with lattice oxygen for O atoms shifts to a lower binding energy of 529.67 eV. This shift, along with the emergence of the In_2O_3/In_2S_3 heterostructure, suggests that the heterojunction formation impacts the chemical environment of In_2O_3, promoting the electron transfer from In_2S_3 to In_2O_3. The binding energies of In 3d and O 1s in In_2O_3/In_2S_3-0.5ZCS remain consistent with those observed in In_2O_3/In_2S_3. Turning to Fig. 2d, the S 2p spectrum of In_2O_3/In_2S_3 reveals two main peaks, centered at approximately 163.06 eV and 161.97 eV, corresponding to S $2p_{1/2}$ and S $2p_{3/2}$, respectively. These peaks align with the typical characteristic peaks of metal sulphides. Interestingly, the binding energy of In_2O_3/In_2S_3-0.5ZCS exhibit a slight decrease compared to that of In_2O_3/In_2S_3, with values of 162.67 eV for the S $2p_{1/2}$ orbitals and 161.49 eV for the S $2p_{3/2}$ orbitals. This decrement signifies the successful construction of the heterojunction, affirming the electronic coupling between In_2O_3/In_2S_3 and ZnCdS. In addition, this observed negative binding energy shift implies an enhancement in the electron density at the In site. Therefore, ZnCdS serves as an electron donor to In_2O_3/In_2S_3. The heterojunction between ZnCdS and In_2O_3/In_2S_3 effectively facilitates this electron transfer, leading to a substantial augmentation in the photocatalytic reaction rate. Fig. 2(e and f) illustrate the resolved spectra of Cd 3d and Zn 2p in In_2O_3/In_2S_3-0.5ZCS. Specifically, Cd 3d is divided into two main peaks with binding energies of about 405.16 eV and 411.92 eV, which can be attributed to Cd $3d_{5/2}$ and Cd $3d_{3/2}$, respectively. Similarly, Zn 2p displays two distinct peaks at around 1121.69 eV and 1144.73 eV, attributed to Zn $2p_{3/2}$ and Zn $2p_{1/2}$, respectively.

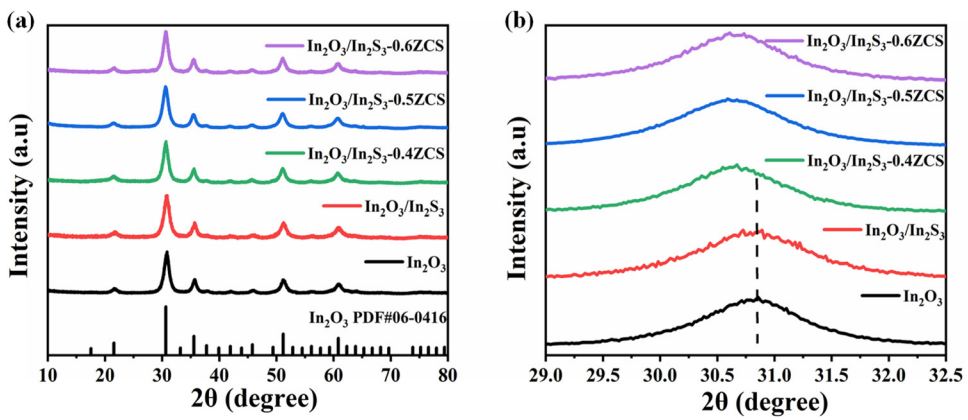

Fig. 1 (a) XRD spectra of In_2O_3, In_2O_3/In_2S_3, In_2O_3/In_2S_3-ZCS photocatalysts; (b) magnified XRD image.

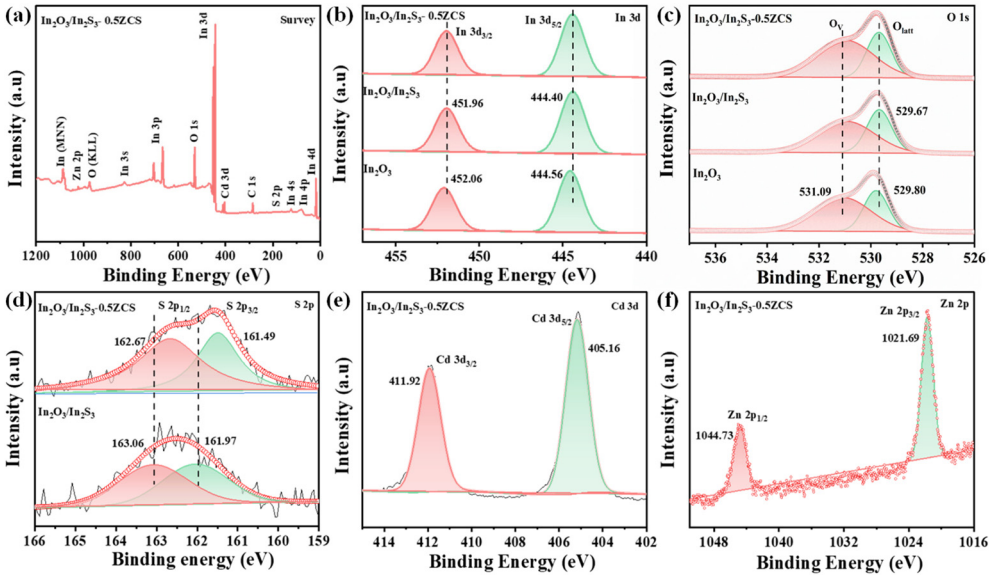

Fig. 2 (a) XPS survey spectra of In_2O_3/In_2S_3-0.5ZCS sample; high resolution XPS of (b) In 3d; (c) O 1s; (d) S 2p; (e) Cd 3d; (f) Zn 2p.

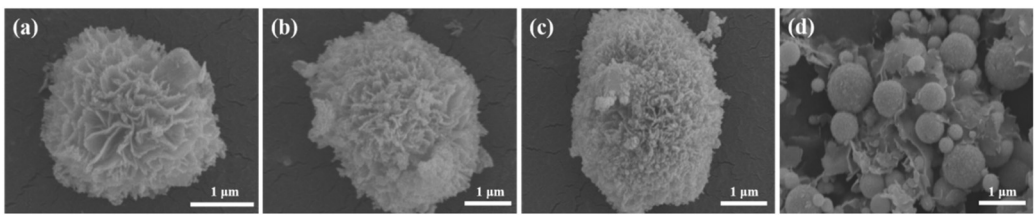

Fig. 3 SEM images of (a) In_2O_3; (b) In_2O_3/In_2S_3; (c) In_2O_3/In_2S_3-0.5ZCS; (d) ZnCdS.

3.2 Morphology and microstructure

To provide a more detailed depiction of the microscopic morphology and compositional structure of pure In_2O_3, In_2O_3/In_2S_3, In_2O_3/In_2S_3-0.5ZCS, and ZnCdS samples, scanning electron microscopy (SEM) images are presented in Fig. 3. The pure In_2O_3, synthesized through a comprehensive process involving hydrothermal treatment, freeze-drying, and calcination, exhibits a spherical flowery structure with a diameter of approximately 2 μm. The surface of pure In_2O_3 is composed of a layer of thin slices, whereas ZnCdS has a small spherical morphology (Fig. 3d). Upon the introduction of in situ grown In_2S_3, the SEM images reveal a transition in the flower-like structure of In_2O_3, becoming roughened and overlaid with a layer of In_2S_3 slices. Subsequently, following the incorporation of $Zn_{0.4}Cd_{0.6}S$, SEM image shows the uniform distribution of $Zn_{0.4}Cd_{0.6}S$ particles on the interlayer surfaces of In_2S_3/In_2O_3. These $Zn_{0.4}Cd_{0.6}S$ particles effectively cover the entire surface of the spherical floral structure, indicating the successful loading of $Zn_{0.4}Cd_{0.6}S$ and corroborating the formation of the In_2O_3/In_2S_3-ZCS heterostructure.

The transmission electron microscopy (TEM) images provide further insights into the morphology of the In_2O_3/In_2S_3-0.5ZCS samples. As depicted in Fig. 4a, the TEM image of In_2O_3/In_2S_3-0.5ZCS microspheres clearly reveal its In_2O_3-like lamellar structure, consistent with the findings from the SEM images. Additionally, Fig. 4b displays the high-resolution TEM (HRTEM) image of In_2O_3/In_2S_3-0.5ZCS, showcasing the heterostructures' morphology and lattice details with remarkable clarity. It is noteworthy that In_2O_3/In_2S_3-0.5ZCS displays three distinct lattice spacings of 0.292 nm, 0.272 nm, and 0.331 nm, corresponding precisely to the (222), (400), and (111) crystal planes of In_2O_3, In_2S_3, and ZCS, respectively. This alignment concurs the X-ray diffraction (XRD) results, validating the successful construction of the In_2O_3/In_2S_3-ZCS heterogeneous structure. Furthermore, Fig. 4(c–h) presents the elemental mapping images of the In_2O_3/In_2S_3-ZCS heterostructure, highlighting the uniform distribution of all elements across the sample. This homogeneity in the elemental distribution underscores the successful synthesis and formation of the In_2O_3/In_2S_3-ZCS heterostructure.

To further explore the specific surface area and pore structure of the In_2O_3, In_2O_3/In_2S_3, and In_2O_3/In_2S_3-0.5ZCS samples, BET testing was conducted. The N_2 adsorption–desorption isotherms of pure In_2O_3, In_2O_3/In_2S_3, and In_2O_3/In_2S_3-0.5ZCS are depicted in Fig. 5, revealing characteristic type IV isotherms (Fig. 5a). Notably, these samples exhibit remarkable adsorption capacity at higher relative pressure

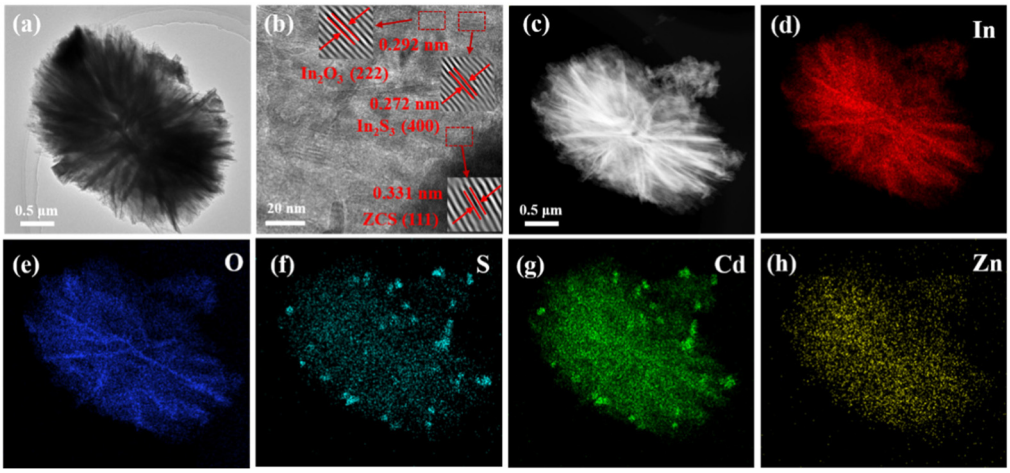

Fig. 4 (a) TEM image of In_2O_3/In_2S_3-0.5ZCS; (b) HRTEM image of In_2O_3/In_2S_3-0.5ZCS; (c–h) elemental mapping images of In, O, S, Cd and Zn of the In_2O_3/In_2S_3-0.5ZCS sample.

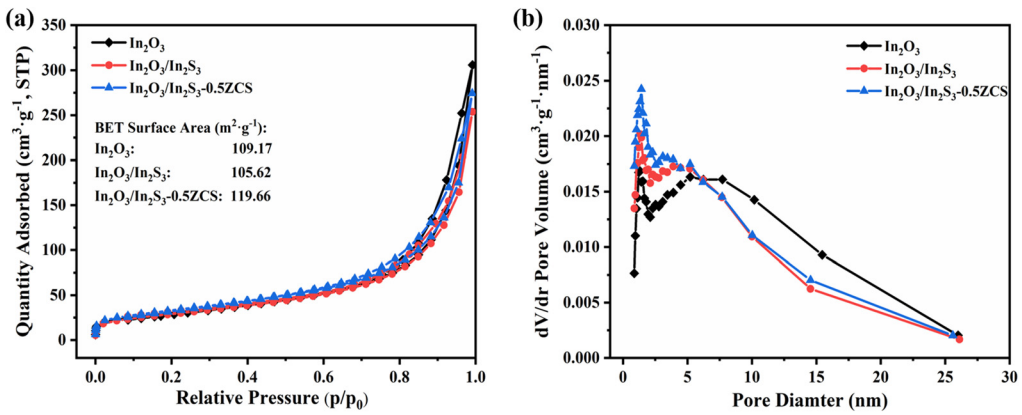

Fig. 5 (a) N_2 adsorption–desorption isotherms; (b) pore size distribution curves of In_2O_3, In_2O_3/In_2S_3 and In_2O_3/In_2S_3-0.5ZCS.

ranges (P/P_0 = 0.8–1), suggesting their porous nature. The specific surface area data reveals that In_2O_3/In_2S_3-0.5ZCS possesses the highest value of 119.66 $m^2\ g^{-1}$, exceeding both In_2O_3/In_2S_3 (105.62 $m^2\ g^{-1}$) and pure In_2O_3 (109.17 $m^2\ g^{-1}$). The decrease in the specific surface area following the introduction of In_2S_3 could potentially be attributed to the incomplete dispersion of In_2S_3 within the pores of In_2O_3, resulting in In_2S_3 flakes covering the surface and obstructing channels. However, after the loading of ZnCdS, not only were the ZnCdS particles interspersed within In_2O_3, but they were also deposited onto the In_2S_3 flakes. This led to an augmentation in the specific surface area of In_2O_3/In_2S_3-0.5ZCS, offering more reaction sites and potentially enhancing the photocatalytic nitrogen fixation performance. Fig. 5b further illustrates that the pore sizes of In_2O_3, In_2O_3/In_2S_3 and In_2O_3/In_2S_3-0.5ZCS are mainly distributed in the range of 2–25 nm, with an average pore size of 10.1 nm, 8.8 nm, and 8.4 nm, respectively, and all of them belong to the mesoporous materials.

3.3 Light absorption capacity and band structure

To investigate the optical absorptivity and energy band structure of the samples, UV-vis diffuse reflectance spectroscopy (UV-vis DRS) was utilized for comprehensive characterization. As illustrated in Fig. 6a, In_2O_3, In_2O_3/In_2S_3, and In_2O_3/In_2S_3-0.5ZCS displayed similar absorption spectra. Notably, in the wavelength range of 550 nm to 800 nm, both In_2O_3/In_2S_3 and In_2O_3/In_2S_3-0.5ZCS exhibited enhanced light absorption compared to In_2O_3. Moreover, near 420 nm, the light absorption of In_2O_3/In_2S_3-0.5ZCS surpassed that of In_2O_3 and In_2O_3/In_2S_3 slightly, potentially attributed to the increased light reflections resulting from the successful heterojunction formation. The bandgap values (E_g) for these three samples were approximately determined by plotting $(\alpha h\nu)^2$ against the photon energy ($h\nu$) using the Kubelka–Munk function. As illustrated in Fig. 6b, the bandgap values (E_g) were calculated to be 2.93 eV, 2.95 eV, and 2.86 eV for In_2O_3, In_2O_3/In_2S_3, and In_2O_3/In_2S_3-0.5ZCS, respectively. Furthermore, the valence band infor-

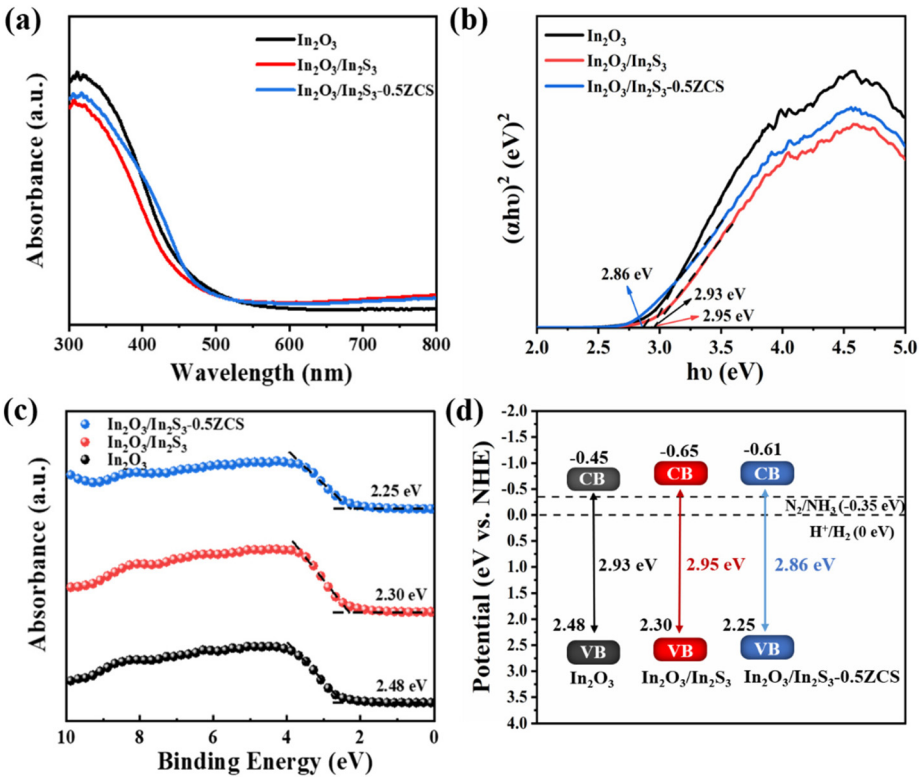

Fig. 6 (a) UV-vis spectra; (b) Tauc plot; (c) XPS valence band spectrum; (d) schematic illustration of the band position for In_2O_3, In_2O_3/In_2S_3 and In_2O_3/In_2S_3-0.5ZCS samples.

mation of the samples was obtained through X-ray photoelectron spectroscopy (XPS) valence band analysis, revealing valence band values of 2.48 eV, 2.30 eV, and 2.25 eV for In_2O_3, In_2O_3/In_2S_3, and In_2O_3/In_2S_3-0.5ZCS, respectively, as shown in Fig. 6c. By combining the results of the valence band energy (E_{VB}) and bandgap energy (E_g), the conduction band potentials (CB) for In_2O_3, In_2O_3/In_2S_3, and In_2O_3/In_2S_3-0.5ZCS were calculated to be −0.45 eV, −0.65 eV, and −0.61 eV, respectively. This analysis indicates that the conduction band position of the anion-exchanged *in situ* growth of part of In_2S_3 shifts to a more negative value, favoring the reduction reaction of N_2. Moreover, the narrower band gap of the In_2O_3/In_2S_3-0.5ZCS sample, compared to In_2O_3, suggests improved photogenerated electron–hole separation and enhanced photocatalytic nitrogen fixation performance. For clarity, the energy band positions of In_2O_3, In_2O_3/In_2S_3, and In_2O_3/In_2S_3-0.5ZCS are visually compared in Fig. 6d.

3.4 Photoelectric chemical properties

Photoluminescence spectroscopy (PL) was utilized to characterize the efficiency of photogenerated electron–hole separation. As depicted in Fig. 7a, the In_2O_3, In_2O_3/In_2S_3, and In_2O_3/In_2S_3-0.5ZCS samples exhibit emission peaks centered around 470 nm, exhibiting a gradual decrease in peak intensity when excited at a wavelength of 370 nm. This trend signifies that the *in situ* growth of In_2S_3, along with the formation of the In_2O_3/In_2S_3-0.5ZCS heterojunction, plays a pivotal role in enhancing the efficiency of photogenerated electron–hole separation. Notably, the In_2O_3/In_2S_3-0.5ZCS sample displays the lowest photoluminescence peak, which could potentially enhance the photocatalytic performance. These findings suggest that the In_2O_3/In_2S_3-0.5ZCS sample achieves the optimal electron–hole separation efficiency, effectively suppressing the recombination of photogenerated electrons and holes. The photogenerated carrier migration and recombination efficiency were further characterized through transient photocurrent spectra and electrochemical impedance spectra (EIS). As illustrated in Fig. 7b, under alternating on/off visible light irradiation, the transient photocurrent response of the In_2O_3/In_2S_3-0.5ZCS sample surpasses those of In_2O_3 and In_2O_3/In_2S_3, indicating its superior carrier migration efficiency and reduced carrier recombination. Fig. 7c presents the corresponding electrochemical impedance spectra (EIS) for the three samples, revealing that the In_2O_3/In_2S_3-0.5ZCS sample exhibits the smallest arc radius, signifying lower electron migration resistance and higher conductivity. This finding further corroborates the efficient charge carrier separation observed in the photoluminescence and transient photocurrent response studies.

3.5 Photocatalytic nitrogen fixation performance

The photocatalytic nitrogen fixation test was conducted using deionized water as the proton source and a 300 W xenon lamp as the light source, all without the use of a sacrificial agent. The NH_4^+ content in the solution was detected using the Nano

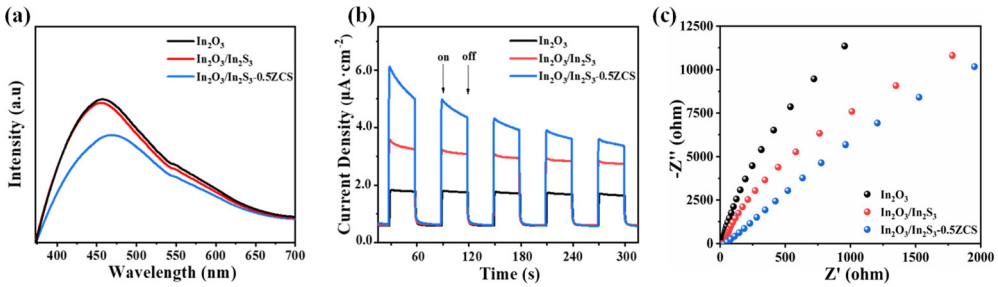

Fig. 7 (a) PL spectra with excitation wavelength of λ = 370 nm; (b) photocurrent responses under visible light; (c) EIS Nyquist plots for In_2O_3, In_2O_3/In_2S_3, and In_2O_3/In_2S_3-0.5ZCS samples.

reagent spectrophotometric method. As evident from the results, the NH_4^+ yields of all samples hovered close to 0 in the absence of illumination. However, upon activating the light source, the NH_4^+ yields of all samples exhibited a steady increase, correlating positively with the duration of light exposure. The average NH_4^+ yields of all samples over a two-hour period are presented in Fig. 8a. The photocatalytic nitrogen fixation activity of the samples followed the specific order of magnitude: In_2O_3/In_2S_3-0.5ZCS > In_2O_3/In_2S_3-0.4ZCS > In_2O_3/In_2S_3-0.6ZCS > In_2O_3/In_2S_3 > In_2O_3. Under light exposure, the In_2O_3 sample exhibited minimal photocatalytic nitrogen fixation performance. However, the In_2O_3/In_2S_3 sample, achieved through the in situ growth of In_2S_3 on In_2O_3 via anion exchange, displayed significantly performance due to the formation of a heterojunction. This heterojunction effectively facilitated the separation of holes and electrons, enhancing carrier migration efficiency and thereby improving photocatalytic nitrogen fixation. Upon further loading $Zn_{0.4}Cd_{0.6}S$ onto the samples, the photocatalytic nitrogen fixation ability was significantly enhanced. Specifically, with the addition of 50 wt% ZCS, the NH_4^+ yield reached 71.2 μmol g^{-1} h^{-1} which was 10.47 times higher than that of In_2O_3 (6.8 μmol g^{-1} h^{-1}) and 3.22 times higher than that of In_2O_3/In_2S_3 (22.1 μmol g^{-1} h^{-1}).

To assess the photocatalytic stability of the In_2O_3/In_2S_3-0.5ZCS sample, five cycles of nitrogen fixation were conducted. Remarkably, even after enduring five consecutive cycles, the NH_4^+ yield of the In_2O_3/In_2S_3-0.5ZCS sample remained steadfast at 50.4 μmol g^{-1} h^{-1}, retaining a commendable 70.79% of the initial NH_4^+ yield. This photocatalytic stability suggests that the In_2O_3/In_2S_3-0.5ZCS photocatalyst possesses good cyclic stability, despite the potential challenges posed bysulfide photocorrosion. Meanwhile, the calculated apparent quantum yields (AQY) of In_2O_3/In_2S_3-0.5ZCS exhibited values of 8.8% at 420 nm, 4.9% at 450 nm, and 1.6% at 500 nm (Fig. 8d), which were consistent with the light absorption in the UV-visible spectrum (Fig. 6a). In order to investigate the photocatalytic NH_4^+ yield under different experimental con-

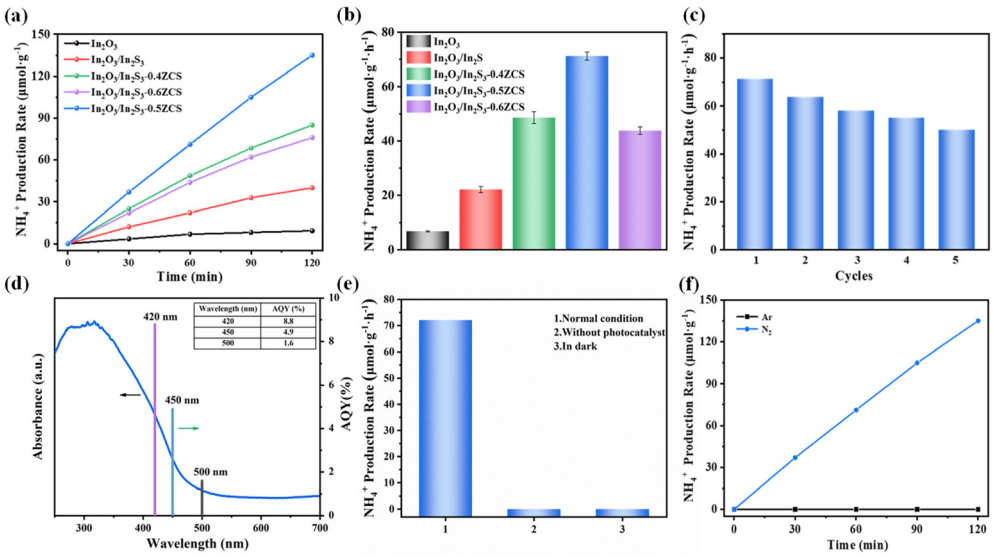

Fig. 8 (a) Time courses of photocatalytic NRR on the as-prepared samples; (b) NH_4^+ production rate of all samples; (c) cycling stability test for NH_4^+ of In_2O_3/In_2S_3-0.5ZCS; (d) wavelength-dependent AQY and DRS spectrum of In_2O_3/In_2S_3-0.5ZCS; (e) photocatalytic NH_4^+ yield of In_2O_3/In_2S_3-0.5ZCS under different conditions; (f) the photocatalytic NH_4^+ yield of In_2O_3/In_2S_3-0.5ZCS in N_2 and Ar.

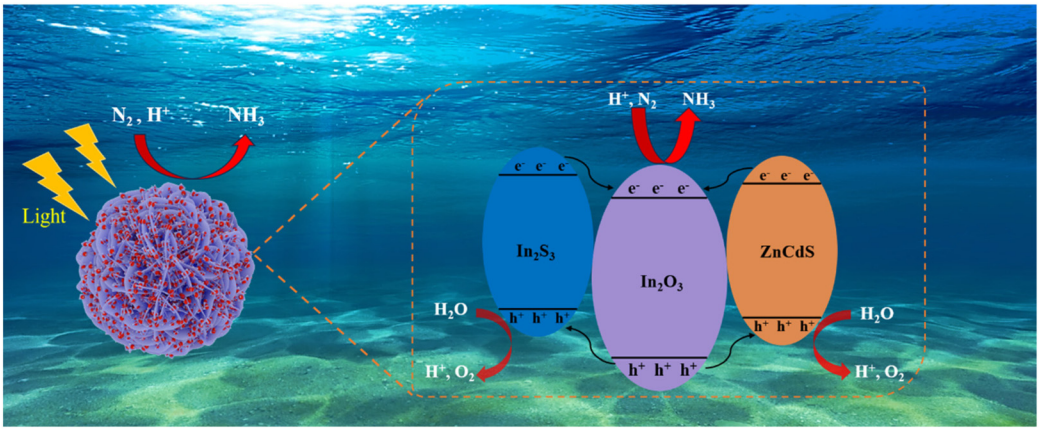

Scheme 2 Possible mechanism of photogenerated charge transfer and induced photocatalytic nitrogen fixation by In_2O_3/In_2S_3-0.5ZCS.

ditions, we evaluated the photocatalytic nitrogen fixation performance of In_2O_3/In_2S_3-0.5ZCS samples, as shown in Fig. 8e. Notably, under both catalyst-free and dark conditions, the NH_4^+ yield remained close to 0. To unequivocally determine that the NH_4^+ in the aqueous solution indeed originated from the introduced N_2 in the reaction system, photocatalytic nitrogen fixation experiments were carried out on the In_2O_3/In_2S_3-0.5ZCS sample, substituting Ar (argon) for N_2. As Fig. 8f clearly illustrates, when N_2 was used as the feedstock gas, the NH_4^+ yield increased almost linearly with increasing light exposure time. Conversely, when Ar was utilized, no NH_4^+ was detected, indicating that the source of NH_4^+ was indeed N_2, and its concentration remained constant with prolonged light exposure. This validates that the nitrogen source for NH_4^+ production in the aqueous solution was indeed the N_2 introduced into the reaction system.

3.6 Photocatalytic nitrogen fixation mechanism

Based on the results obtained from the material characterization, photoelectrochemical performance, and nitrogen fixation performance tests, we postulate a photocatalytic nitrogen fixation mechanism, as illustrated in Scheme 2. When exposed to the incident light, the valence band electrons of In_2O_3 photocatalyst undergo excitation and transition to the conduction band. The in situ grown In_2S_3 plays a crucial role in adjusting the conduction band potential to a more negative state, thereby facilitating redox reactions on the photocatalyst's surface. Additionally, the incorporation of ZnCdS creates heterojunctions, which not only narrows the forbidden band but also enhances the transport of photogenerated electrons. According to XPS analysis, ZCS and In_2S_3, which possess a significant number of catalytically active sites, exhibit rapid activation under light exposure, resulting in the generation of photogenerated electrons and holes. These electrons predominantly migrate towards the In_2O_3 surface with a lower conduction band value to catalyze the reduction of incoming nitrogen to ammonia. Meanwhile, the In_2O_3 holes migrate to the surfaces of ZCS and In_2S_3, where they are consumed by water. This continuous migration and consumption of charge carriers predominantly efficient separation during the photocatalytic nitrogen fixation reaction. This structural design not only enhances the spatial separation of photogenerated carriers but also prevents excessive recombination, thereby significantly improving the performance of the photocatalytic nitrogen fixation process.

4. Conclusion

In conclusion, the study successfully synthesized In_2O_3/In_2S_3-ZCS ternary heterojunctions via a facile method. This involved depositing In_2S_3 sheets onto the In_2O_3 surface through a simple in situ anion exchange process, followed by decorating the structure with ZnCdS particles using a low-temperature hydrothermal method. The resulting In_2O_3/In_2S_3-ZCS composite exhibited remarkable photocatalytic activity, achieving an NH_4^+ yield of 71.2 μmol g^{-1} h^{-1}, which surpassed the performance of In_2O_3 (6.8 μmol g^{-1} h^{-1}) by a factor of 10.47 and In_2O_3/In_2S_3 (22.1 μmol g^{-1} h^{-1}) by 3.22 times. This exceptional photocatalytic nitrogen fixation efficiency can be attributed to the ternary heterostructure, which effectively hinders the recombination of photogenerated electron–hole pairs and enhances interfacial charge transfer. Moreover, the heterojunction interface formed between CdZnS, In_2S_3, and In_2O_3 facilitates electron transport, supplying an ample number of electrons to In_2O_3, thus significantly enhancing the photocatalytic nitrogen fixation efficiency. This research provides valuable insights for the design and construction of ternary heterojunctions in the field of photocatalytic nitrogen fixation.

Data availability

The authors confirm that the data supporting the findings of this study are available within the article and its ESI.† For any questions or clarifications regarding the data, please contact the corresponding author.

Conflicts of interest

There are no conflicts to declare.

Acknowledgements

This work was financially supported by the National Natural Science Foundation of China (Grant No. 21975229 and 52072350).

References

1 P. Li, Z. Zhou, Q. Wang, M. Guo, S. Chen, J. Low, R. Long, W. Liu, P. Ding, Y. Wu and Y. Xiong, *J. Am. Chem. Soc.*, 2020, **142**, 12430–12439.
2 M. Cheng, C. Xiao and Y. Xie, *J. Mater. Chem. A*, 2019, **7**, 19616–19633.
3 B.-H. Wang, G.-H. Chen, B. Hu, L. Chen, X. Wang, S. Tian, X.-S. Hu, Y. Li, C. Peng and S.-F. Yin, *EES Catal.*, 2024, **2**, 180–201.
4 P. Qi, X. Gao, J. Wang, H. Liu, D. He and Q. Zhang, *RSC Adv.*, 2022, **12**, 1244–1257.
5 Q. Hao, C. Liu, G. Jia, Y. Wang, H. Arandiyan, W. Wei and B.-J. Ni, *Mater. Horiz.*, 2020, **7**, 1014–1029.
6 H. Liu, *Chin. J. Catal.*, 2014, **35**, 1619–1640.
7 H. Li, C. Mao, H. Shang, Z. Yang, Z. Ai and L. Zhang, *Nanoscale*, 2018, **10**, 15429–15435.
8 Q. An, M. McDonald, A. Fortunelli and W. A. Goddard III, *J. Am. Chem. Soc.*, 2020, **142**, 8223–8232.
9 T. Oshikiri, K. Ueno and H. Misawa, *Angew. Chem., Int. Ed.*, 2014, **53**, 9802–9805.
10 J. Deng, J. A. Iñiguez and C. Liu, *Joule*, 2018, **2**, 846–856.
11 M. H. Vu, M. Sakar, S. A. Hassanzadeh-Tabrizi and T. O. Do, *Adv. Mater. Interfaces*, 2019, **6**, 1900091.
12 R. Li, *Chin. J. Catal.*, 2018, **39**, 1180–1188.
13 B. Hu, B.-H. Wang, L. Chen, Z.-J. Bai, W. Zhou, J.-K. Guo, S. Shen, T.-L. Xie, C.-T. Au, L.-L. Jiang and S.-F. Yin, *ACS Catal.*, 2022, **12**, 11860–11869.
14 R. Michalsky, B. J. Parman, V. Amanor-Boadu and P. H. Pfromm, *Energy*, 2012, **42**, 251–260.
15 H. Hirakawa, M. Hashimoto, Y. Shiraishi and T. Hirai, *J. Am. Chem. Soc.*, 2017, **139**, 10929–10936.
16 G. Zhang, C. D. Sewell, P. Zhang, H. Mi and Z. Lin, *Nano Energy*, 2020, **71**, 104645.
17 Y. Sun, Y. Ahmadi, K.-H. Kim and J. Lee, *Renewable Sustainable Energy Rev.*, 2022, **170**, 112967.
18 G. Zhang, X. Yang, C. He, P. Zhang and H. Mi, *J. Mater. Chem. A*, 2020, **8**, 334–341.
19 P. Praus, *ChemistrySelect*, 2023, **8**, e202204511.
20 G. Li, W. Yang, S. Gao, Q. Shen, J. Xue, K. Chen and Q. Li, *Chem. Eng. J.*, 2021, **404**, 127115.
21 L.-Y. Chen and W.-D. Zhang, *Appl. Surf. Sci.*, 2014, **301**, 428–435.
22 Z. Wang, C. Hou, Q. De, F. Gu and D. Han, *ACS Sens.*, 2018, **3**, 468–475.
23 P. Rai, J.-W. Yoon, C.-H. Kwak and J.-H. Lee, *J. Mater. Chem. A*, 2016, **4**, 264–269.
24 M. Meng, X. Wu, X. Zhu, L. Yang, Z. Gan, X. Zhu, L. Liu and P. K. Chu, *J. Phys. Chem. Lett.*, 2014, **5**, 4298–4304.
25 W. Liu, J. Zhang, Q. Kang, H. Chen and R. Feng, *Ecotoxicol. Environ. Saf.*, 2023, **252**, 114611.
26 X. Huang, R. Du, Y. Zhang, J. Ren, Q. Yang, K. Wang, Y. Ni, Y. Yao, R. A. Soomro, L. Guo, C. Yang, D. Wang, B. Xu and F. Fu, *J. Colloid Interface Sci.*, 2024, **664**, 33–44.
27 F. Zhang, X. Li, Q. Zhao and D. Zhang, *ACS Sustainable Chem. Eng.*, 2016, **4**, 4554–4562.
28 M. Liu, P. Li, S. Wang, Y. Liu, J. Zhang, L. Chen, J. Wang, Y. Liu, Q. Shen, P. Qu and H. Sun, *J. Colloid Interface Sci.*, 2021, **587**, 876–882.
29 P. Chang, Y. Wang, Y. Wang and Y. Zhu, *Chem. Eng. J.*, 2022, **450**, 137804.
30 B. Hu, B.-H. Wang, Z.-J. Bai, L. Chen, J.-K. Guo, S. Shen, T.-L. Xie, C.-T. Au, L.-L. Jiang and S.-F. Yin, *Chem. Eng. J.*, 2022, **442**, 136211.
31 Y.-X. Tan, Z.-M. Chai, B.-H. Wang, S. Tian, X.-X. Deng, Z.-J. Bai, L. Chen, S. Shen, J.-K. Guo, M.-Q. Cai, C.-T. Au and S.-F. Yin, *ACS Catal.*, 2021, **11**, 2492–2503.
32 F. Zhang, X. Li, Q. Zhao and A. Chen, *J. Phys. Chem. C*, 2016, **120**, 19113–19123.
33 J. Yang, X. Zhu, Z. Mo, J. Yi, J. Yan, J. Deng, Y. Xu, Y. She, J. Qian, H. Xu and H. Li, *Inorg. Chem. Front.*, 2018, **5**, 3163–3169.
34 H. Xu, Y. Wang, X. Dong, N. Zheng, H. Ma and X. Zhang, *Appl. Catal., B*, 2019, **257**, 117932.
35 S. Lin, S. Li, H. Huang, H. Yu and Y. Zhang, *Small*, 2022, **18**, e2106420.
36 E. Ha, S. Ruan, D. Li, Y. Zhu, Y. Chen, J. Qiu, Z. Chen, T. Xu, J. Su, L. Wang and J. Hu, *Nano Res.*, 2021, **15**, 996–1002.
37 W. Zhang, S. Zhao, H. Qin, Q. Zheng, P. Zhang, X. Li, C. Li, T. Wang, N. Li, S. Zhang and X. Xu, *Sci. China Mater.*, 2022, **66**, 1042–1052.
38 Y. Zhao, R. Shi, X. Bian, C. Zhou, Y. Zhao, S. Zhang, F. Wu, G. I. N. Waterhouse, L.-Z. Wu, C.-H. Tung and T. Zhang, *Adv. Sci.*, 2019, **6**, 1802109.
39 J. Yu, S. Xiong, B. Wang, R. Wang, B. He, J. Jin, H. Wang and Y. Gong, *Colloids Surf., A*, 2023, **656**, 130481.
40 H. Cheng, B. Huang, X. Qin, X. Zhang and Y. Dai, *Chem. Commun.*, 2012, **48**, 97–99.